

A basic swimmer at low Reynolds number

Marco Leoni

Università degli Studi di Milano, Dip. Fisica
and INFN, sez. Milano, Via Celoria 16, 20100 Milano, Italy
and

University of Cambridge, Cavendish Laboratory
and Nanoscience Center, JJ Thomson Avenue, CB3 0HE Cambridge, UK.

Jurij Kotar

University of Cambridge, Cavendish Laboratory
and Nanoscience Center, JJ Thomson Avenue, CB3 0HE Cambridge, UK.

Bruno Bassetti

Università degli Studi di Milano, Dip. Fisica
and INFN, sez. Milano, Via Celoria 16, 20100 Milano, Italy

Pietro Cicuta

University of Cambridge, Cavendish Laboratory
and Nanoscience Center, JJ Thomson Avenue, CB3 0HE Cambridge, UK.
E-mail: pc245@cam.ac.uk

Marco Cosentino Lagomarsino

Università degli Studi di Milano, Dip. Fisica
and INFN, sez. Milano, Via Celoria 16, 20100 Milano, Italy.
E-mail: marco.cosentino@unimi.it

Swimming and pumping at low Reynolds numbers are subject to the “Scallop theorem”, which states that there is no net fluid flow for time reversible motions. Microscale organisms such as bacteria and cells are subject to this constraint, and so are existing and future artificial “nano-bots” or microfluidic pumps. We study a very simple mechanism to induce fluid pumping, based on the forced motion of three colloidal beads through a cycle that breaks time-reversal symmetry. Optical tweezers are used to vary the inter-bead distance. This model is inspired by a theoretical swimmer proposed by Najafi and Golestanian [Phys.Rev. E, 69, 062901, 2004], but in this work the relative softness of the op-

tical trapping potential introduces a new control parameter. We show that this system is able to generate flow in a controlled fashion, characterizing the model experimentally and numerically.

1 Introduction

Insight into swimming of microorganisms and bacteria can be gained by studying the motion at low Reynolds numbers of experimental and theoretical model systems [1, 2]. Compared to the macroscopic world, a striking feature of propulsion of these micron-scale objects, for which inertia is typically negligible, is that

a body striving to move has to change its shape with time in a non-reciprocal fashion [3]. For example, swimming of a magnetically driven semi-flexible artificial filament was recently demonstrated, by a wave-like motion similar to flagella [4]. In this work we realize a much simpler system which uses only two effective degrees of freedom, the distances between central and lateral spheres. This is inspired by a 3-bead linear chain theoretical model [5] which has never been realized experimentally.

2 Materials and Methods

2.1 Optical tweezers

The optical tweezers setup used in this work consists of a laser (IPG Photonics, PYL-1-1064-LP, $\lambda=1064\text{nm}$, $P_{max}=1.1\text{W}$) focused through a water immersion objective (Zeiss, Achromar IR 63x/0.90 W), trapping from below. The laser beam is steered via a pair of acousto-optic deflectors (AA Opto-Electronic, AA.DTS.XY-250@1064nm) controlled by custom built electronics, allowing multiple trap generation with sub-nanometer position resolution. Instrument control and data acquisition are performed by custom software. The trapping potential is locally described by a harmonic spring, and the trap stiffness was calibrated by measuring the thermal displacements of the trapped beads. The trapping stiffness of the central bead in this work is $k_{\text{trap}} = 4.1 \pm 1.3 \text{ pN}/\mu\text{m}$, whereas the external beads were held more strongly, with $k_{\text{trap, external}} = 8.1 \pm 1.4 \text{ pN}/\mu\text{m}$. The errors quoted here are the standard deviation over several independent experiments, with the same beads and same tweezers configuration. They could also be a source for the slight discrepancy in relaxation times seen in 2(a) and (b). The sample is illuminated with a halogen lamp and is observed in bright field with a fast CMOS camera (Allied Vision Technologies, Marlin F-131B). Silica beads of $3.0\mu\text{m}$ diameter (Bangs Labs) were diluted to extremely low concentration to avoid any spurious bead falling into the laser trap. The set of three trapped beads was floated well above the glass slide surface (at

about 10 times the bead diameter) to minimize any hydrodynamic drag from the solid surface. Except where specified differently, we used a solution of glycerol (Fisher, Analysis Grade) 51% by weight in water (Ultrapure grade, ELGA) which has a viscosity of 6.23 mPa s [6]. Experiments were performed at 25°C .

2.2 Experimental protocol

The experimental protocol is composed of two parts. In the first calibration stage all the traps are kept at rest, and the beads undergo only Brownian motion confined by the traps. The driven dynamics occurs only during the second stage. Data is acquired at 48.79 frames per second, with exposure time $19 \times 10^{-3}\text{s}$. A run lasts ten minutes, during which we collect about 30000 frames, equally divided between calibration and dynamics. We collected 4 runs for each set of parameters. Images are analysed using a correlation filter with a kernel optimized to the bead profile, followed by a 2-d least-square fit. This gives the center-of-mass coordinates of the beads in each frame with an error of the order of $10^{-3}\mu\text{m}$.

2.3 Numerical simulations

Numerical simulations were performed by integrating directly the equation of motion of the three beads with Taylor's method [7]. We considered both simulations that included thermal motion (i.e. adding a white noise term to the equations) and deterministic ones, finding no relevant differences. The results in the body of the paper mainly refer to the deterministic model.

3 Experimental

We study a swimmer composed of three beads immersed in a high viscosity Newtonian liquid. The beads are controlled by an optical tweezer [8, 9] and interact with each other through the fluid. The laser traps are set-up following the scheme of figure 1(a,b). The central trap is kept at rest, holding the central bead in a

soft harmonic potential of stiffness k_{trap} , while the lateral ones switch between two positions. By forcing the lateral beads to move, we implement the four time-reversal symmetry breaking phases shown in figure 1a.

Two of the parameters that characterize the system are purely geometric: ϵ , the maximum oscillation amplitude for the lateral beads, and d , the distance between the laser positions at the starting phase of the cycle. Their physical interpretation is that ϵ sets the strength of the stroke, while d sets the magnitude of the hydrodynamic interaction. The additional parameter is τ , the switching time of the laser, which corresponds to the temporal length of each phase in the cycle. Finally, the viscosity η , which is set in the preparation of the sample, characterizes the fluid, the hydrodynamic interactions, and the amplitude of thermal motion. The former parameters, together with the radius R of the beads, characterize completely the system.

Despite its simplicity, the model encapsulates all the essential characteristics of a swimmer. We study the flow generation on the fluid, using the central bead as a probe. This corresponds to studying the propulsion of a freely moving swimmer. By tracking the position of the central bead it is possible to detect a left-right symmetry breaking and quantify the net flow at varying parameters.

3.1 Quantifying displacements

Trapping lasers act with good approximation as harmonic potentials on each bead. Thus, the average displacement $\langle \Delta x \rangle_t$ of the central bead from the position of the central trap can be converted using Hooke's law into the mean force exerted on the fluid by the whole system. However, a direct measurement of $\langle \Delta x \rangle_t$ is at the limit of experimental resolution. The limiting factor is not the imaging resolution, but the presence of thermal fluctuations. This thermal noise can be compensated by longer sampling, however to reduce this error down to the nanometer scale would require experiments 10^2 times longer than ours, which is not prac-

tical*. Instead, we quantify the flow using a different approach. The electronically controlled trap movement temporization allows to precisely keep track of the phase within each cycle. We can therefore average over the repeated realizations, and reconstruct the mean dynamic cycle of the beads. It is significant to focus on the central one, in the stationary trap: An example of mean cycle for this bead is shown in figure 2(a), where four peaks due to the lateral motion are clearly visible. These peaks correspond to the maximum displacement of the central bead in each phase of the motion. The configurations of the three traps are indicated schematically in the bottom panel of figure 2(a). Due to the different dispositions of the outer beads, the drags the central bead is subject during each phase are different and cause unequal displacements. Our method characterizes the pumping by means of the asymmetry of the peaks. On the mean cycle, we label p_1, p_2, p_3, p_4 (in order of decreasing value) the peaks in the displacement, and we define the following observables, devised to quantify the asymmetry of the motion: (1) $\delta_{inv} := (p_1 - p_2) - (p_4 - p_3)$, the difference between the lower and the upper peak values, (2) $\delta_2 := p_1 - p_4$, the difference between the upper and the lower maximum peak values. For an illustration we refer to the mid panel in figure 2(a). The reason for using both definitions (1) and (2) to quantify asymmetry is the fact that the mean cycles have different shapes for different values of τ . For example, in the case of small values of τ , the intermediate peaks are not well distinguished, as shown in the top panel of figure 2(a). Thus, we adopt the observable δ_2 which makes use of the upper and the lower maximum peak values only. In the opposite case of high values of τ , see bottom panel of figure 2(a), the four peaks are well defined, and it is more effective to use the observable δ_{inv} . The advantage is that δ_{inv} is determined independently from the equilibrium position x_0 , which is needed for δ_2 and cannot be measured during the active motion. Thus, it allows for more direct measurements. These

*Already at times of the order of a few tens of minutes there can be sources of mechanical noise leading to drift.

observables lack a simple physical meaning and should rather be thought as order parameters useful in characterizing the asymmetry of the peaks. Both these quantities change sign by reverting the sequence of steps and allow to verify if the system behaves as expected, pumping in the opposite direction. We also define a third observable (3) $s := |p_1| + |p_2| + |p_3| + |p_4|$, the sum of absolute values of the peaks. s is always positive, and quantifies the amplitude of the swimmer's motion.

3.2 Comparison of experiments with simulations

We compare the measured flow to simple numerical simulations (see methods). The hydrodynamic interaction between the spheres is described by the Oseen tensor [10], corresponding to the limit of point force, or far field. Along the \hat{x} axis of the swimmer, the equation of motion for bead n is

$$\dot{x}_n = \frac{1}{\gamma} \left(F_n + \sum_{n \neq m} \left(\frac{3R}{2r_{nm}} \right) F_m \right)$$

with $n, m = 1, 2, 3,$ (1)

where $\gamma = 6\pi\eta R$ is Stokes' drag, F_i is the external force exerted on the i -th particle, and r_{nm} indicates the relative distance between the n and m . The experimental values of η and k_{trap} were used in the simulations.

As can be seen by inspecting figure 2(b), the observed relaxation times are shorter in the experimental data of bead motions than in the simulations at corresponding parameters. To exclude possible errors, we performed the following tests. First, we simulated a single particle in a stationary trap, including thermal fluctuations, calculated the relaxation time in the time autocorrelation function. For an isolated particle, the relaxation time is the ratio k_{trap}/γ . Using the experimental values in the simulations, we found excellent agreement for beads both in pure water and water/glycerol. Subsequently, we compared the simulation (with and without thermal noise) to the experiment for one trapped particle in water/glycerol, in a trap undergoing repeated displacements, see

figure 2(c). Also in this case, the simulation and experiment match very well. In conclusion, there is excellent agreement in the single particle regime, confirming experimental calibration and numerical methods. Therefore the slight discrepancy in the three-bead data must be due to the excessively simple theoretical description of multiple interacting bodies [†]. In other words, the flow induced by each bead is not perfectly represented by a linear superposition of single-particle Oseen propagators [10]. This is not surprising, considering that this is a long-distance, or far-field approximation. A common procedure to correct for this effect makes use of a perturbative expansion in the parameter R/d . We checked this by implementing the first and second perturbative corrections [13, 14] in our simulations, finding very similar quantitative results as with the Oseen tensor. The reason for this is that the parameter R/d is not small, being of the order of $1/3$, so that the real dynamics is not accessible perturbatively [‡]. Despite this limit, the simulations do allow us to compare the experimental results with a prediction for the net force, or flow, generated in the fluid by the swimmer. A mapping between each of the observables (δ_2 , δ_{inv}) and the temporal average $\langle \Delta x \rangle_t$ is obtained by means of simulations. Here, sampling problems are not present and $\langle \Delta x \rangle_t$ is quantifiable directly by time averaging with arbitrary accuracy; δ_2 and δ_{inv} are obtained from the steady-state mean cycle, similarly to experiments. For both δ_2 and δ_{inv} , we verify that there exists a one to one mapping with $\langle \Delta x \rangle_t$. We use this relation to associate as a function of ϵ each point of the experimental curve to the corresponding mean displacement, obtaining $\langle \Delta x \rangle_t$ as a function of ϵ that is converted into a mean force via Hooke's law. The

[†]Note that we can exclude that inertia and the propagation time of hydrodynamic interaction plays a role, as deviations were found to be at the nano-second scale [11, 12], well outside from the time scales of our experiments.

[‡]While approaches that do not make use of the explicit form of the solution of hydrodynamic equations [15, 16] may help solving this problem, in general, to compensate for this small discrepancy one would have to solve Stokes' equation with the proper boundary conditions [17].

procedure is illustrated in Figure S1 of supplementary methods.

4 Discussion

Our first result is that the system is able to generate flow. This is qualitatively visible in the distribution of position of the central bead (figure 1(c)). This effective potential is composed of two contributions: the harmonic potential exerted by the tweezer, and the configurational bias induced by the interaction with the lateral moving beads. The latter contribution causes the emergence of two effective asymmetric minima. This asymmetry can be quantified accurately using the above-defined observables (figure 3). Simulations show that there exists a one-to-one map between δ_{inv} and δ_2 , and the values for the mean force, so that it is possible to convert δ_{inv} and δ_2 directly to forces. For fixed values of τ , we ran a series of experiments to characterize the dependence of the mean position from the displacements ϵ of the lateral beads. Figure 1(b) shows one of the two possible time-reversal breaking sequences. By reverting the sequence into the specular one, the swimmer should move in the opposite direction. Experimentally, we implemented both sequences, and found that this property holds. Figure 3(a) shows a comparison between the experimental and simulated observable δ_{inv} as a function of ϵ . The absolute value of the corresponding mean force is shown in figure 3(b). The maximum mean forces reached in our experiments are of the order of 0.03pN, roughly corresponding to a net swimming/pumping speed of about $0.2\mu\text{m/s}$. Note that this force is exceedingly small to be measured with an optical tweezer using conventional techniques, which has posed a barrier in past investigations [18]. The indirect technique used here enables to overcome this barrier, and can possibly be useful in different contexts.

It is interesting to study the influence of τ , by fixing the value of ϵ , and in figure 3(c) we plot the propulsion force at varying τ , compared with simulations. In both cases there is a good quantitative agreement between the model with

Oseen interactions and the experimental data. By increasing the distance d between the beads, the asymmetry in the peaks becomes more difficult to detect. However it is still possible to characterize the dependence of fluid pumping on the parameter d by using the amplitude variable s . In figure 3(d), s is plotted versus the distance, for both simulations and data. In both cases this quantity decays as $1/d$. Quantitatively, there is a small systematic deviation between experiment and simulations. The $1/d$ decay directly depends on hydrodynamic interactions, and can be understood with a simple argument on the maximum deviation of an initially resting trapped bead subject to the perturbation induced through the fluid by another bead at distance d relaxing for a stretch ϵ in another harmonic potential (see Supplementary Material for further details).

4.1 Comparison with other model systems

It is instructive to compare our swimmer with the closely related theoretical model originally proposed in the literature [5] by Najafi and Golestanian, and the variants that have been recently explored [19, 20]. There are two main features characterizing our model. Firstly, beads are subject to the compliance of the trapping potentials. The original Najafi-Golestanian swimmer has rigid links. More recently, the model has been solved for the case of chemical transitions between states [19] and for general bead and link sizes and imposed deformations [17, 20]. However, an actuated movement by quadratic potentials has not been addressed explicitly in the previous literature. While the behavior of the simplest rigid Najafi-Golestanian swimmer is essentially characterized by the ratio ϵ/d [5, 21], more general models can have more complex dynamics, imposed by additional relevant time or length-scales. Our system is also subject to an additional parameter, the ratio $\frac{\tau}{\tau_0}$, with $\tau_0 := \gamma/k_{\text{trap}}$ of the imposed displacement time to the characteristic relaxation time of the bead. Hence the phenomenology of our system depends also on the ratio of the two time scales.

The most important consequence is that our simulations show a power-law dependence of the speed, or mean force, on ϵ , with an exponent that increases monotonically with increasing τ , slightly larger than the quadratic law found for the Golestanian swimmer. Experimentally, it is problematic to measure incontrovertibly this scaling, due to the large errors in the fit for the exponents, whose average values, however, do exceed two. In the limiting case of small τ , the two models behave in the same way. This can be understood in the following way. Assume for simplicity that the lateral forcing beads can be described as free particles relaxing through the minimum of a harmonic potential. Their position follows a simple temporal law governed by an exponential decay $x(t) \sim x_0 \exp(-t/\tau_0)$, and accordingly the velocity $v(t) \sim (x_0/\tau_0) \exp(-t/\tau_0)$. For small values of τ , the ratio τ/τ_0 is small ensuring that the velocity of the trapped bead does not decay significantly during each step in the cycle, being a constant proportional to τ_0 as in the Najafi Golestanian swimmer, where the beads have a constant displacement velocity [5]. On the other hand, our results confirm that in the small τ limit the mean force scaling with ϵ/d is compatible with a quadratic law. This regime is also the one where the swimmer's propulsion is optimal. In the numerical experiments, the fitted exponents we find are consistently larger than 2 (between 2.12 and 2.41). However, the predicted trend with ϵ cannot be confirmed experimentally because of the large errors (Supplementary Figure S2). The second difference with the original Najafi-Golestanian swimmer is that our swimmer is not intrinsic, but actuated by external forces [4, 22]. In particular, the total actuating force is not null instantaneously, but only over a cycle. This has been shown to lead to qualitatively distinct behavior in other systems [23]. In our case, using simulations of an analogous intrinsic swimmer actuated by two-body two-state springs, we find that the differences are mostly quantitative, the intrinsic variant being slightly faster and more efficient (Supplementary Figure S3).

Finally, it may be of interest to compare this pump to other engines. We can estimate the

dissipation rate in our pump to be between 0.5×10^{-17} and 4×10^{-17} J/s, which is comparable to an *E. coli* bacterium swimming in water [24]. The efficiency of this pump is of the order of $10^{-3}\%$ (calculated as the ratio of the mean output to input power) which is lower than for typical biological systems such as *E. coli* [1, 25]. These results are important on fundamental grounds and for applications in nano-scale machines.

Acknowledgments. We thank Ray Goldstein, Christopher Lowe and Ignacio Pagonabarraga for useful comments and discussion. This work was supported by the Korea Foundation for International Cooperation of Science & Technology (KICOS) through a grant provided by the Korean MOST (No.2007-00338) and by the UK EPSRC.

References

- [1] Berg, H. *Physics Today* **53**, 24 (2000).
- [2] Buchanan, M. *Nature Phys* **4**, 83 (2008).
- [3] Purcell, E. *Am J Phys* **45**, 3–11 (1977).
- [4] Dreyfus, R. *et al.* *Nature* **437**, 862–5 (2005).
- [5] Najafi, A. & Golestanian, R. *Phys Rev E Stat Nonlin Soft Matter Phys* **69**, 062901 (2004).
- [6] Weast, R. C. & Astle, M. J. *CRC Handbook of Chemistry and Physics, 60th Ed.* (CRC Press, Boca Raton, 1979).
- [7] Cosentino Lagomarsino, M., Jona, P. & Bassetti, B. *Phys Rev E* **68**, 021908 (2003).
- [8] Ashkin, A. *Proc Natl Acad Sci U S A* **94**, 4853–60 (1997).
- [9] Block, S. M. *Nature* **360**, 493–5 (1992).
- [10] Doi, M. & Edwards, S. *The Theory of Polymer Dynamics* (Clarendon Press, Oxford, 1986).
- [11] Henderson, S., Mitchell, S. & Bartlett, P. *Phys Rev Lett* **88**, 088302 (2002).
- [12] Atakhorrami, M., Koenderink, G. H., Schmidt, C. F. & MacKintosh, F. C. *Phys Rev Lett* **95**, 208302 (2005).
- [13] Rotne, J. & Prager, S. *J Chem Phys* **50**, 4831 (1969).
- [14] Batchelor, G. *J Fluid Mech* **119**, 379 – 408 (1982).
- [15] Mazur, D. & Bedeaux, P. *Physica* **76**, 235–246 (1974).
- [16] Liverpool, T. B. & MacKintosh, F. C. *Phys Rev Lett* **95**, 208303 (2005).
- [17] Alouges, F., DeSimone, A. & Lefebvre, A. *J Nonlinear Sci* (2007). DOI 10.1007/s00332-007-9013-7.
- [18] Riveline, D., Wiggins, C., Goldstein, R. & Ott, A. *Phys Rev E* **56**, R1330 – R1333 (1997).
- [19] Golestanian, R. & Ajdari, A. *Phys Rev Lett* **100**, 038101 (2008).
- [20] Golestanian, R. & Ajdari, A. *Phys Rev E* **77**, 036308 (2008).
- [21] Earl, D. J., Pooley, C. M., Ryder, J. F., Bredberg, I. & Yeomans, J. M. *J Chem Phys* **6**, 126 (2007).
- [22] Cosentino Lagomarsino, M. C., Capuani, F. & Lowe, C. P. *J Theor Biol* **224**, 215–24 (2003).
- [23] Lauga, E. *Phys Rev E Stat Nonlin Soft Matter Phys* **75**, 041916 (2007).
- [24] Bustamante, C., Liphardt, J. & Ritort, F. *Physics Today* **58**, 43 (2005).
- [25] Chattopadhyay, S., Moldovan, R., Yeung, C. & Wu, X. L. *Proc Natl Acad Sci* **103**, 13712 (2006).

Fig. 1 Experimental realization of the low Reynolds number swimmer, and proof of force generation. (a) Scheme of the lasers' disposition during a single phase of motion, in which the active traps (green) act on the beads as harmonic potentials. The parameters ϵ and d are sketched. (b) Sequence of snapshots of the experiment showing four time-symmetry breaking steps in the basic cycle. Crosses indicate the active laser trap positions. By moving the lateral beads and keeping the central one at rest, it is possible to study the flow generated on the fluid, using the central bead as a probe. A left-right asymmetry in its position signals that flow is generated. Top panel: starting configuration, where the distances between beads take their maximum values. (c) Two-dimensional map of the effective potential felt by the central bead. The plot is obtained by taking the logarithm of the relative frequencies of the positions occupied by the central bead during 500 repetitions of the basic cycle. The colour scale indicates in dark the most frequent position. The map shows a left-right symmetry breaking (the left-hand minimum is deeper), which is a proof of the mean generated flow in the system.

Fig. 2 Reconstruction of the mean cycle. The experiment is a sequence of repetitions of the elementary cycle illustrated in figure 1. By treating each period as a single realization and averaging over all realizations, one recovers the mean cycle of the dynamics, averaged over the thermal fluctuations due to Brownian motion in the fluid. (a) Detail of the mean cycle for the central bead (\diamond with errorbars) compared with simulations (solid lines) for different τ . The plot reports the longitudinal displacement coordinate of each bead as a function of the cycle phase in the interval $(0, 2\pi)$. The peaks become more defined as τ increases. Top panel: $\tau = 40$ ms ; middle panel: $\tau = 80$ ms ; bottom panel: $\tau = 320$ ms. The position of the four peaks and the traps' configuration in the four phases of the cycle are illustrated in the middle and bottom panel respectively. (b) Mean cycle for the whole system (three beads). The longitudinal displacement coordinate of each bead is plotted as a function of time. Dotted lines correspond to experimental values for the left bead (black), the central bead (red) and the right bead (green). These are compared with the results of numerical simulations (solid lines with the same color code). (c) Close up and complete cycle showing relaxation of a single bead in a switching trap, with no interacting partners.

Fig. 3 Quantitative characterisation of the swimmer. The main observable is the mean force felt by the central bead, measured by its mean displacement in the optical trap. The mean force is studied here as a function of the parameters ϵ and τ . (a) shows δ_{inv} as a function of the lateral amplitude ϵ , comparing experimental values (triangles) with simulation (continuous line). There are two possible time-reversal-symmetry breaking cycles, corresponding to the two opposite pumping directions. By temporally reversing the cycle showed in figure (1), δ_{inv} changes sign, showing that the direction of pumping can be controlled. The following panels show experimental data (\diamond) compared to simulations (continuous line). Each \diamond represents the average over 4 different experiments and the error bars correspond to the standard deviations of the four values. (b) Shows the mean force (obtained from the observable δ_{inv} and numerical simulations) as a function of ϵ , for $d = 6\mu\text{m}$, $\tau = 80$ ms, $\eta = 6.23$ mPa.s. (c) Mean force as a function of τ . Here the other experimental parameters are $d = 6\mu\text{m}$, $\epsilon = 1\mu\text{m}$, $\eta = 6.23$ mPa.s. (d) Amplitude of motion as a function of d . Increasing d the force becomes weaker and difficult to detect, and we have to use the amplitude parameter s to compare with simulations. The measured and simulated values of s scale as d^{-1} (as discussed further in the Supplementary Material).

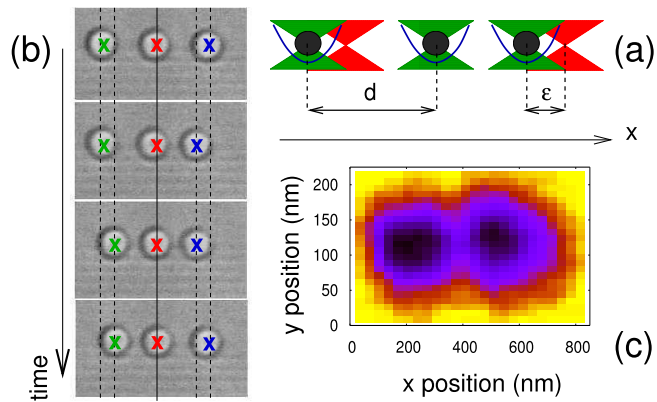


Figure 1: Experimental realization of the low Reynolds number swimmer, and proof of force generation.

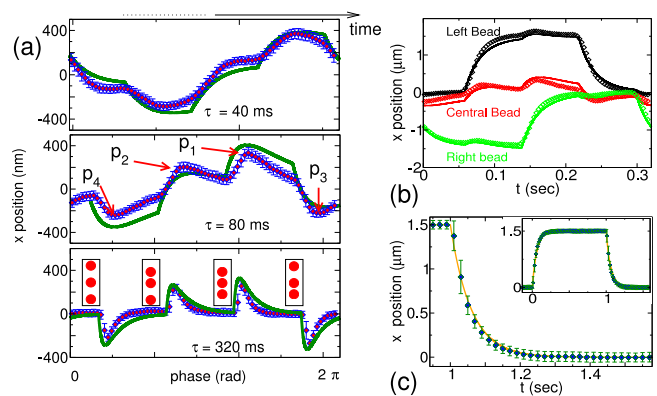


Figure 2: Reconstruction of the mean cycle.

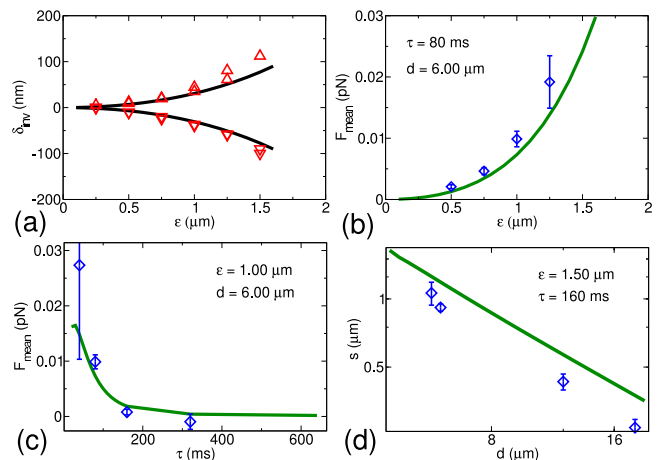


Figure 3: Quantitative characterisation of the swimmer.

SUPPLEMENTARY MATERIAL

Additional considerations on the model and the data analysis

Scaling with d

We present here a simple argument for the scaling of the amplitude s with distance d , explaining the scaling seen for experiments and simulations in figure 3(d).

To estimate the d -dependency of the amplitude during a cycle, it is sufficient to describe the displacement of the central bead in one of the four sub-phases. We consider the simplified but physically equivalent situation of two interacting trapped beads at distance d . Initially the left bead, which represents the central bead in the experiment, is at rest and the right bead is out of its equilibrium position by a distance ϵ , as it would be if in the instant the trap has been shifted. The initial conditions are thus $x_L(0) = 0, x_R(0) = d$ and the equilibrium positions of the trapping potentials are $x_{0,L} = 0; x_{0,R} = (d - \epsilon)$. To a first approximation, (“zeroth order” in R/d) the left bead is still, and the position of the right bead follows a simple relaxation law

$$x_R^{(0)}(t) = \epsilon \left(e^{-\frac{t}{\tau_0}} - 1 \right) + d \quad . \quad (2)$$

This unperturbed solution can be used to estimate (by the force balance with the fluid) the source of force $F_R^{(0)} = -k_{\text{trap}}(x_R^{(0)} - d)$ applied by the right bead on the fluid during its relaxation. This can then be used into equation (1) of the main text for the left bead, giving

$$\tau_0 \dot{x}_L^{(1)} = x_L^{(1)} - \frac{3R}{2d} x_R^{(0)} \quad , \quad (3)$$

where $x_R^{(0)}$ appears as an external perturbation, and we approximated the distance between the beads with d , which is justified in the limit of large distances $d \gg \epsilon$. With this assumption, the problem becomes linear and the solution to order R/d can be calculated as

$$x_L^{(1)}(t) = \frac{3R\epsilon}{2d} \frac{t}{\tau_0} e^{-\frac{t}{\tau_0}} \quad . \quad (4)$$

In turn, this solution could be used as a source for the equation for x_R , to obtain hierarchically the higher order contribution in R/d to its motion. The value of the peak of the central bead in the experiment s can be estimated by the maximum displacement of the left bead

$$x_{L,\text{max}}^{(1)} = \frac{3R\epsilon}{2de} \quad . \quad (5)$$

This argument implies that the leading order scaling of each peak in a cycle, and hence of s , is $1/d$. The argument has the advantage of showing how the hydrodynamic interaction tensor comes

into play explicitly after a trap switches its position.

In the same linear approximation, the coupled equations (eq.1) from the main text can even be solved directly in a straightforward way, and the resulting maximum displacement is:

$$x_{L,\max} = \frac{3R\epsilon}{2d} \frac{1}{\left(1 + \frac{3R}{2d}\right)^{1+\frac{2d}{3R}}} , \quad (6)$$

which has the same behavior in the limit of large d/R .

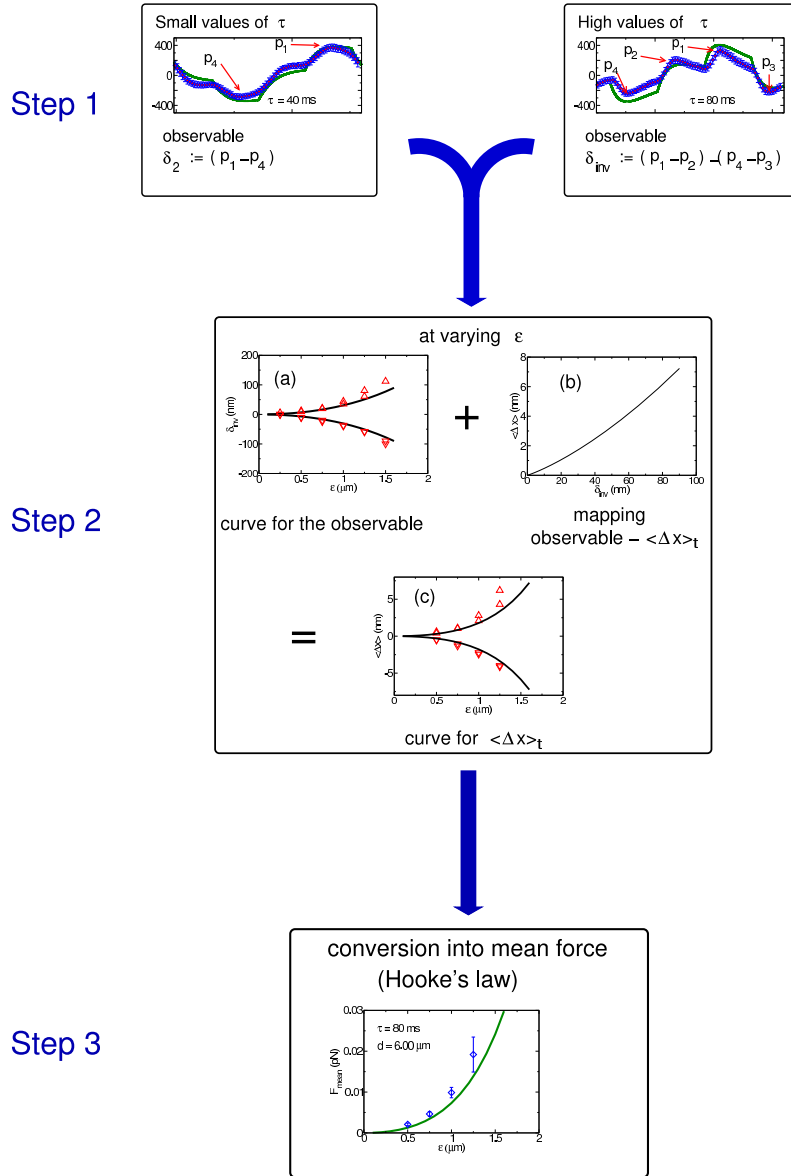
Strictly speaking, this result is applicable in the regime $\tau \gg \tau_0$, in which the beads have the time to fully relax in the trap potentials. In the opposite limit, $\tau \ll \tau_0$, since the subcycle ends while the central bead is still moving away from the center of its trap, the maximum position can be estimated using the same solution, $x_L^{(1)}(t)$, by the position assumed by the central bead at the end of this subcycle, i.e. the instant $t = \tau$. Thus as

$$x_{L,\max}^{(1)} = \frac{3R\epsilon}{2d} \frac{\tau}{\tau_0} e^{-\frac{\tau}{\tau_0}} , \quad (7)$$

and the scaling with d is unaffected.

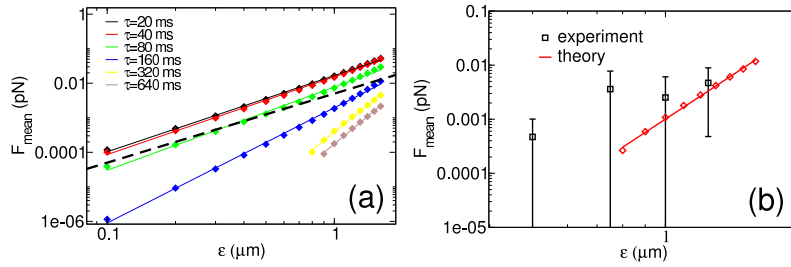
Relating the observables δ_2 and δ_{inv} with the mean force.

We summarise here how the procedure to relate the experimental data to the induced flow.



Supplementary Figure S1: **Converting observables into mean force.** This scheme illustrates the procedure used to obtain the mean force from the experiments, by means of simulations. Step 1: Because of the different shapes of the mean cycles for different values of τ , we define two different observables δ_2 and δ_{inv} to quantify the asymmetry in the displacements for the central bead. The peaks which enter in the definitions are indicated with red arrows. Step 2: (a) We analyze the mean cycle of experiments and simulations, extracting each observable at varying ϵ . We also calculate directly the temporal average $\langle \Delta x \rangle$ for the position of the central bead. (b) Comparing these results and eliminating the dependence from ϵ , we find that there exist a one to one mapping between each observable and the temporal average $\langle \Delta x \rangle$. (c) Using this relation the curve of each observable as a function of ϵ can be converted into a curve of the mean position as a function of ϵ . Step 3: using Hooke's law we convert the mean displacement into a mean force as a function of ϵ .

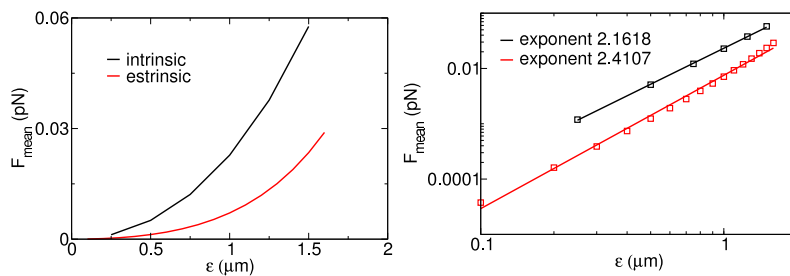
Scaling with τ



Supplementary Figure S2: **Scaling law for the mean force at varying τ .** (a) Plot on log-log scale of the simulated mean displacement from the equilibrium position of the central bead. The curve is a power law with different exponents for different values of τ . In our model the exponent varies, and increases monotonically for increasing τ . In the limit of small τ the mean displacement follows a power law with exponent close to 2 (dashed line), which resembles the behavior of the Golestani swimmer. (b) Comparison between experimental and theoretical data for $\tau = 320$ ms on log-log scale. Due to the large error bars on the experimental curve, the determination of the exponent from the experiment is subject to large uncertainties.

Intrinsic Swimmer

Figure S3 shows a comparison of our model with simulations of an analogous intrinsic swimmer.



Supplementary Figure S3: **Comparison of the propulsive forces for extrinsic and intrinsic swimmers.** The extrinsic swimmer is studied experimentally and numerically in this work, whereas we can only study the intrinsic swimmer, actuated by two-state springs, numerically. The plot shows the mean force with varying ϵ , for simulations of the two models, with parameters $d = 6\mu\text{m}$ $\tau = 80\text{ms}$. The difference between the two swimmers is only quantitative.